Solid Freeform Fabrication 2018: Proceedings of the 29th Annual International Solid Freeform Fabrication Symposium – An Additive Manufacturing Conference
Reviewed Paper

microCLIP Ceramic High-resolution Fabrication and Dimensional Accuracy Requirements

Henry Oliver T Ware*, Cheng Sun*

*Department of Mechanical Engineering, Northwestern University, Evanston, IL 60201

Abstract

Ceramics have been broadly used as structural and functional materials with a wide range of engineering applications. Recent introduction of Continuous Liquid Interface Production (CLIP) uses projection UV photopolymerization and oxygen inhibition to tremendously reduce fabrication time. In addition to 3D printing polymeric materials, it has demonstrated the feasibility of fabricating 3D ceramic parts using photo-curable ceramic resins. However, the associated ceramic particle light-scattering significantly alters the process characteristics of the CLIP process, resulting in broadening of the lateral dimensions in associated with the reduction in the curing depth. Varying the exposure conditions to accommodate the scattering effect further affects the deadzone thickness, which introduces a systematic defocusing error to further complicate the process control. In this work we show that careful characterization and balance of both effects yields an optimal set of process parameters (UV Power and stage speed) for high-resolution 3D fabrication with a given photo-curable ceramic resin.

Introduction

Ceramics are an important class of materials that are used in several industries ranging from aerospace to automotive to biomedicine.[1] Ceramics typically possess high melting temperature, chemical inertness, and great hardness and strength.[1, 2] Ceramic parts can be used in industry as either as a fully sintered ceramic or as a composite with a polymer matrix, dependent on application.[1] A problematic property of ceramic materials are that they can be brittle, making them difficult to machine and require forming methods such as moldings or Additive Manufacturing (also known as 3D printing) to create the green body.[1-3] The green body includes both the ceramic and binder material. For a full ceramic part, the green body is then placed into a high temperature oven, where the binder is burned away from the part, and the ceramic particles become fused together.[1, 4, 5] For the ceramic composite, the green body is the end of the process.

Additive manufacturing methods have recently been used a forming method for specialty ceramic parts where standard forming methods could be difficult.[3] Additive manufacturing describes several processes including extrusion methods, selective laser sintering, and photopolymerization methods.[1, 3-9] Photopolymerization 3D printing methods include stereolithography and inkjet printing. Both methods utilize a slurry with ceramic distributed within a photopolymer material. With the introduction of ceramics into the photopolymer, there is a scattering element within the light path during polymerization. This ceramic particles redirect the incoming UV energy laterally, which affects dimensional accuracy.[3, 10] Characterization of the axial curing depth as well as scattering induced lateral broadening is important when utilizing stereolithography with ceramics, especially for precision high resolution requirements.

CLIP process represents a 3rd generation of the stereolithography process. This process through oxygen diffusion within the UV light path creates a rapid, continuous fabrication method. [2, 11-13] This process creates uniform crosslinked parts, with no layering-related adhesion defects in the final parts. The addition of oxygen diffusion into the light path adds another aspect

to consider when using CLIP-based methods to fabricate polymer and ceramic parts. Standard curing depth and scattering are dependent on total energy dosage during UV exposure.[14] Oxygen deadzone thickness is largely dependent on UV power density (or photon flux).[11] Oxygen dead zone thickness decreases with increasing UV power density as well as with individual layer exposure time.[2, 11] Assuming the resin bath and build platform start from an initial calibrated position, variation of oxygen dead zone could affect the focus of the projected image when curing occurs. This de-focus can affect lateral dimensional accuracy of both pure-polymer resin and ceramic-filled resin products when attempting to fabricate at high resolution.

This work intends to show the relationship of UV Power, stage speed, and ceramic concentration on axial and lateral fabrication accuracy from microCLIP.

Materials and Methods

Materials

Fabrication inks for microCLIP 3D printing process consisted of 1-6 hexanediol diacrylate (HDDA, primary monomer) [Sigma], N,N dimethyl formamide (DMF, solvent), hydroxyapatite (HA, diameter $\leq$ 200nm), Irgacure 819 (photoinitiator), and Triton X (surfactant). Irgacure 819 and Triton X were held constant at 2.2wt.% and 3wt.%, respectively for all tested inks. HA concentration was varied from 0 to 40wt.% and DMF concentration was varied, such that, DMF and HA held a ratio of 3:5. HDDA concentration within each ink was dependent on the other constituent components. All weight percentages listed were in terms of the full ink mixtures.

Fabrication

All parts were fabricated via microCLIP process (Figure 1a). The system utilizes 365nm UV light to induce polymerization. UV power density for all experiments fell within the range 2.31mW/cm^2 to 17.055mW/cm^2, corresponding to 25% and 100% system power, respectively. System projected lateral resolution at image focal plane is 7.1um x 7.1um. Oxygen permeable Teflon AF2400 film with 40um thickness acted as our system's transparent optical window, with ambient air as the oxygen source to allow continuous fabrication. Layer slice thickness (LST) for all parts was held constant at 5um. All part designs were created in SolidWorks CAD software.

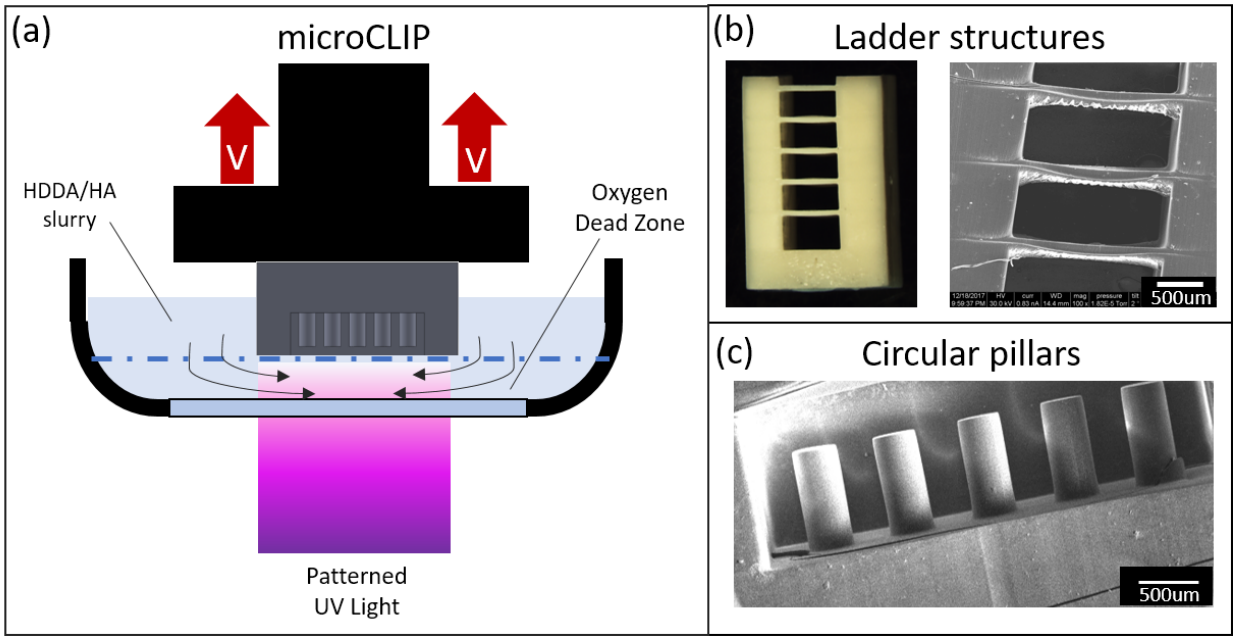

Figure 1: (a) microCLIP schematic. (b) SEM micrograph of axial curing ladders. (c) SEM micrograph of circular pillar array for lateral characterization.

Axial Working Curves and Speed Working Curves

Axial (Curing Depth) working curves for all inks were obtained through fabrication of 'ladder' structures (Figure 1b). In the fabrication of the "ladder" structures, UV power density (P_D) was held constant while platform speed (v_s) was varied. Ladder spokes consisted of 20 fabrication layers. Ladder spoke thickness was analyzed to determine average curing depth via SEM (FEI NOVA600). Axial Working Curves were utilized to determine axial dimensional accuracy. Axial curing depth was fit via the standard stereolithography curing depth equation [14]

$$C_D = D_p ln\left(\frac{E_{max}}{E_c}\right) \quad (1)$$

$$C_D = D_p ln\left(\frac{P_D}{P_c}\right) \quad (2)$$

where D_p is the depth of UV penetration and E terms being the max energy dosage and critical dosage (E_{max} and E_c, respectively). P_D and P_C represent the user controlled UV power density and critical power density, respectively. Average exposure time was calculated from the stage speed (v_s) divided by the layer slice thickness (LST). We defined axial dimensional accuracy (axial critical speed) to be when the average curing depth (C_D) equaled the layer slice thickness (5um). This signified when the rate of curing equaled v_s. The dimensionally accurate (axial critical) speeds were plotted against the UV power density, which we defined as our speed working curves for our full system power range.

Oxygen Deadzone Thickness

Oxygen deadzone thickness was measured by polymerizing a single exposure onto a silicon wafer piece. Exposure pattern was a 3mm x 3mm square. The silicon wafer was separated from the Teflon AF 2400 film by either a 100um or 200um shim. The 200um shim was utilized for the

Pure HDDA (0% HA) resin, while the 100um shim was used for the ceramic-infused resins. The oxygen deadzone was determined at the minimum exposure at which the fabricated layer attached to the silicon wafer. Structure thickness was measured via a digital micrometer. Oxygen deadzone thickness was obtained from subtracting the printed structure thickness from the shim thickness.

Lateral Curing Tests

To determine lateral dimensional accuracy, circular pillars with diameter of 70 pixels were printed (Figure 1c). Intended diameter was 497um. Lateral curing tests were performed at the axial critical speeds obtained from the axial curing depth tests to ensure that all inks had a given curing depth of 5um per layer. Excess curing width (C_w) was obtained through the following equations [3]:

$$C_w = \frac{W_a - W_p}{2} \quad (3)$$

$$C_w = B_w \ln\left(\frac{P}{P_{wc}}\right). \quad (4)$$

In Equation 3, W_a represents the actual measured feature width and W_p is the projected feature width. Equation 4 represents the fitting equation for lateral curing width. In the lateral fit equation, the B_w is the slope, known as the broadening width, with P being the user-specified UV power density and P_{wc} being the power density at onset of excess exposure. P_{wc} allowed determination of the lateral dimensional accurate condition (lateral critical UV power density).

Pixel-wise lateral dimension modeling

2D pixel-wise modelling was performed to approximate the experimentally fabricated 70-pixel diameter lateral curing width. Projection intensity profiles were approximated using the formula:

$$P_{tot} = \sum_{i=1}^{n} P_i \quad (5)$$

where P_i is the UV power density of each individual pixel. Pixels representing pure HDDA polymer in the model were set with a pixel pitch of 6.92um separation and a Gaussian width of 5um. The power density profile width was measured with profile boundary endpoints being the experimentally obtained P_c values. P_c was determined from the axial working curves by dividing the E_c by the average exposure time per layer. Individual pixels could have their Gaussian width and intensities adjusted to approximate scattering or loss of projection focus.

Results

Axial Curing

Initial working curves for all inks were obtained at 2.31mW/cm^2 (corresponding to 27% system intensity), which are shown in Figure 2a. Dimensionally accurate condition was defined when the curing depth matched the layer slice thickness (red line, Figure 2a). From the working curves it can be observed with increasing HA concentration, the ink's intrinsic properties D_P and E_C decrease, typically. With 40% HA, the D_P and E_C falls intermediate of the tested inks. E_c in these working curves indicate the energy necessary to overcome the oxygen deadzone thickness. In addition, with increasing HA, the necessary axial critical energy dosage increases (0.615 to 2.4mW/cm^2) and the corresponding axial critical curing speed decreases (18.8 to 4.7um/s). Axial

critical speeds were obtained for all inks at the following UV power densities: 2.31, 5.8, 9.218, and 17.055mW/cm^2. These measurements yielded our speed working curves, dimensionally accurate speeds with respect to UV power density (Figure 2b). For inks with HA concentration between 0 and 20%, the axial critical curing speeds have an approximately linear relationship to the UV power density. This implies that a single working curve can approximate the full tested region of UV power density and speed combinations. For inks with [HA] greater than 20%, the speed working curves resemble a logarithmic relationship to UV power density.

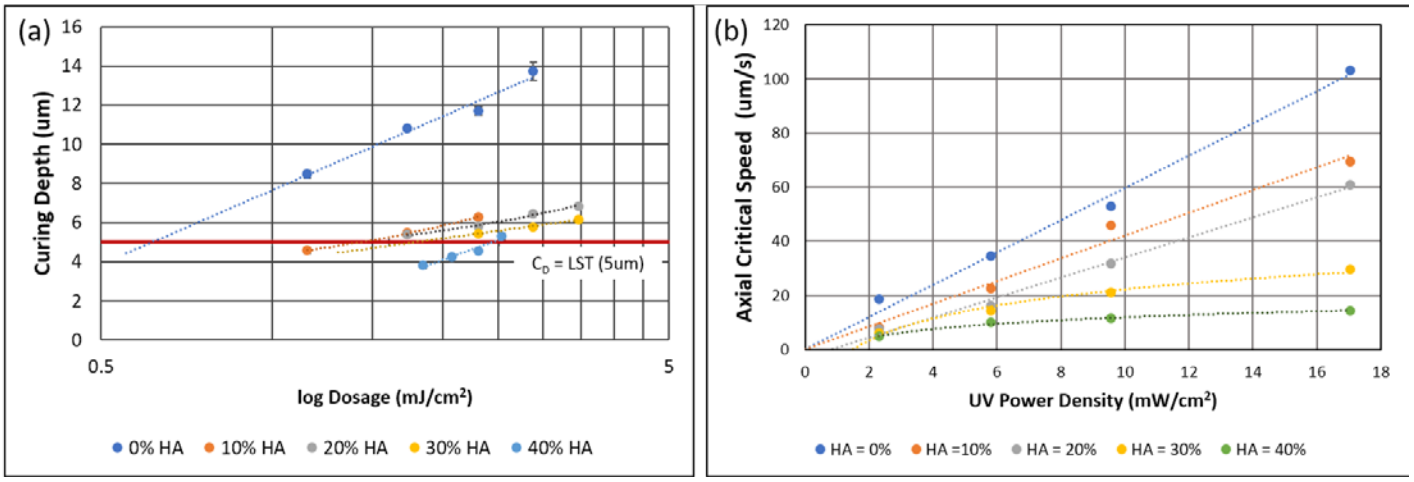

Figure 2: (a) Axial working curves for all tested inks at 2.31mW/cm^2. Ideal curing speed or "dimensionally accurate" speed was determined where the working curves matched LST (red line). (b) Speed working curves for all tested inks across all tested UV power densities.

Oxygen Deadzone Thickness

Pure HDDA is more easily polymerized than its ceramic-infused counterparts. Oxygen appears to be readily diffusible in the pure HDDA ink, with HDDA having the largest deadzone thickness of the tested inks for all tested UV intensities. Deadzone thickness followed a similar trend as described by Tumbleston et.al., where thickness decreased with increasing UV power.[11] Figure 3 below shows the measured oxygen deadzone thickness values corresponding to 2.31%, 5.8, 9.218, and 17.055mW/cm^2 system UV power density. Largest deadzone thickness for pure HDDA was 85.5um. and smallest thickness was measured to be ~12um. The ink consisting of 20% HA featured the second highest deadzone thickness for all tested UV Power density values. Largest deadzone thickness of the 20% HA ink was measured to be 40um and smallest thickness was measured to be 11um. All other ceramic inks were comparable to one another at all tested intensities. Largest deadzone thicknesses for 10%, 30%, and 40% HA inks were measured to be 29, 22, and 25um, respectively. Smallest deadzone thicknesses measured were 8, 8, and 7um, respectively.

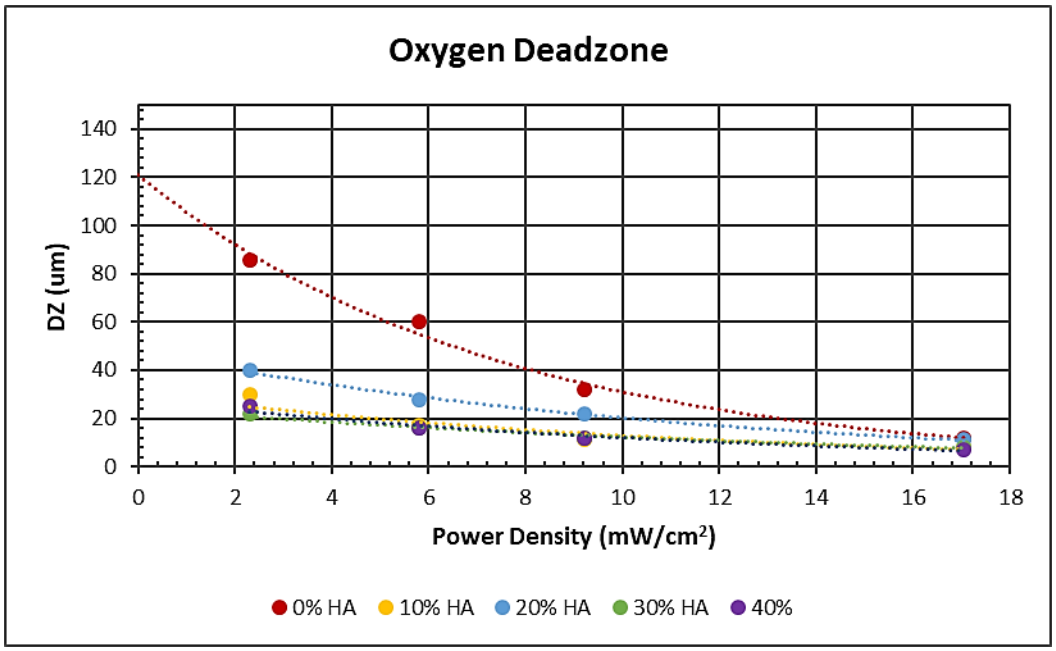

Figure 3: Oxygen Deadzone thickness vs UV Power Density graphs for all tested inks.

Pixel-wise lateral curing scattering model

After experimental data collection was obtained, Matlab was utilized to approximate the cured voxel shape. To ensure energy was conserved, with increasing HA concentration, the individual pixel P_i's were reduced and Gaussian widths ($\square_b$) increased such that the max total power density matched the measured UV power density (17.055mW/cm^2) and the power density profile width was within $\pm$ 3% of the experimental curing widths. Figure 4a & 4b show the increase of Gaussian width and power density decrease, respectively, with increasing HA concentration. The change between pure HDDA and 10% HA ink was very small (in terms of both gaussian width and individual pixel power density), whereas for [HA] > 10% the changes in cured voxel properties are significant. Gaussian width of approximated cured voxels increases in an exponential relationship to HA concentration. Individual pixel penetrative power decreases in a logarithmic relationship to HA with [HA] > 10%. Figure 4c shows our approximated relative cured voxel (represented 2D planar) shapes to approximate ceramic-induced scattering (reduction of intensity and lateral redirection of the energy). Figure 4d shows the experimental and modeled lateral feature with for fabricated 70 pixel diameter circular pillars.

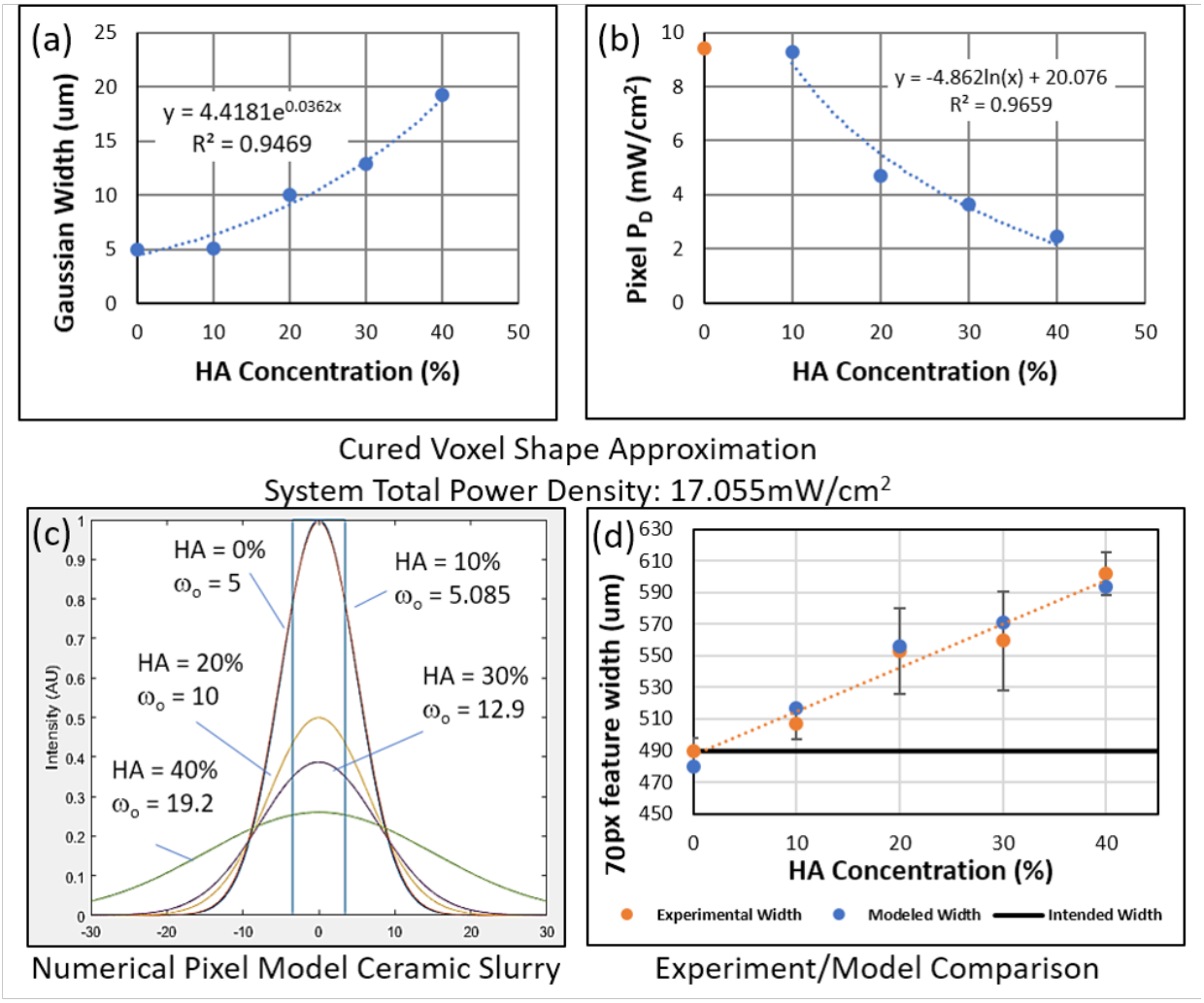

Figure 4: (a) Gaussian width change with increasing [HA]. (b) Individual pixel intensity change with increasing [HA]. (c) Individual relative 2D voxel shape approximation. (d) Experimental lateral curing of 69-pixel feature at 17.055mW/cm² power density and modeled lateral curing feature with increasing [HA].

Pixel-wise lateral curing dead zone -defocus model

While scattering is the primary reason for dimensional deviation, the oxygen dead zone can affect lateral dimensional accuracy. Lateral curing of HDDA ink (0% HA) was 1st analyzed to help determine effect of oxygen dead zone without particle-induced scattering on lateral dimensional accuracy. It could be observed that at full system power density (17.055mW/cm2), the lateral feature size had very good fidelity to the projected image. Full system power density corresponded to the minimum oxygen deadzone thickness for all tested inks. With decreasing intensity (increasing deadzone thickness), the feature lateral dimension also decreased. Where scattering is intrinsic to the ceramic concentration within the ink, oxygen dead zone affects lateral curing via projection edge pixel blurring during the curing process. Pixel-wise intensity profiles were made to approximate the lateral feature size of the 0% HA ink with varied UV power densities (Fig. 5a). Gaussian width of all pixels was set to a constant 5um and pitch between pixels

was 6.92um. To match the experimentally obtained feature widths, for decreasing intensity, pixels on the outside of the distribution had to be gradually decreased from full pixel intensity to 0mW/cm^2. Figure 5b shows the experimentally measured feature size of the HDDA ink, as well as the pixel-wise approximation. The secondary Y-axis of Figure 5b denotes the number of unaltered pixels with respect to UV intensity. With increasing power density, the number of full intensity pixels (denoted as unaltered pixels) also increases (48, 58, 63, 70 pixels for 2.31, 5.8, 9.218, and 17.055mW/cm^{2,} respectively).

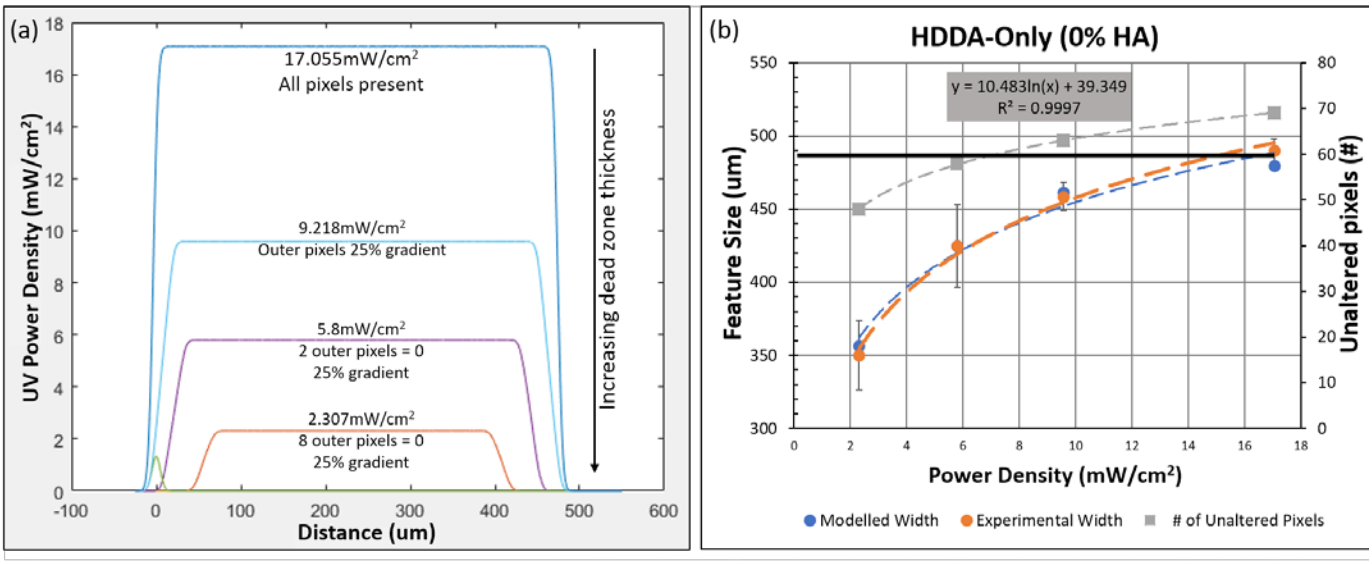

Figure 5: (a) 1-D Intensity profile model for pure HDDA Ink (0% HA) at varying power densities. Also notes pixels intensities that were modeled and taken out. (b) Experimental lateral curing of 69-pixel feature from pure HDDA ink and modeled lateral curing feature with increasing power density (P_D).

Lateral Curing Experimental (All Tested Inks)

The axial critical exposure conditions were utilized to help determine ceramic lateral curing from UV exposure. Figure 6a shows the excess curing width (C_w) of all tested inks at each ink's axial critical speed. There are two competing factors which affect the lateral dimensional accuracy: scattering and the oxygen deadzone-related image blurring. The X-axis in the C_w graph represents dimensional accuracy, with the (+) X-axis representing scattering-dominated lateral deviation and (-) X-axis being deadzone-dominated lateral deviation. Table 1 shows important lateral curing values for the tested inks. The lateral broadening coefficient (B_w) of inks with [HA] > 10% increases with increasing HA percentage. The lateral critical UV power density (P_{wc}) typically decreases with increasing HA, except 40% HA. The P_{wc} of the 40% HA ink ultimately falls between 10% and 20% HA inks. To next obtain the ideal curing speed (v_{wc}, dimensionally accurate axial and lateral curing), we input the P_{wc} value into the speed working curves obtained previously. The ideal curing speed (Figure 6b) shows a very large decrease from pure HDDA (0% HA) to 10% HA ink. The change from 10% HA and above is much more gradual. As shown in Table below, the ideal curing energy dosage (E_{wc}), which is the lateral critical UV power density (P_{wc}) multiplied by the axial critical speed at that intensity (v_{wc}) increases with increasing HA concentration, which is expected. Figure 6c and 6d show 3D printed Luneburg lenses made from 20% HA ink. Figure 6c shows (on left) a Luneburg lens that was printed at the 9.218mW/cm^2 and

31.8um/s. This exposure, while axially dimensionally accurate (5um curing depth), caused enough lateral scattering that the Luneburg lens print resulted in a nearly solid structure. Figure 6c shows (on right) a sputter coated Luneburg lens printed at the ideal curing conditions (6.93mW/cm2 and 22.7um/s). This resulted in a structure that resembled the intended design. Struts of the Luneburg lenses were intended to be 60um and 100um in width. Figure 6d shows an SEM micrograph of the top section of the Luneburg lens and shows good agreement with the intended design.

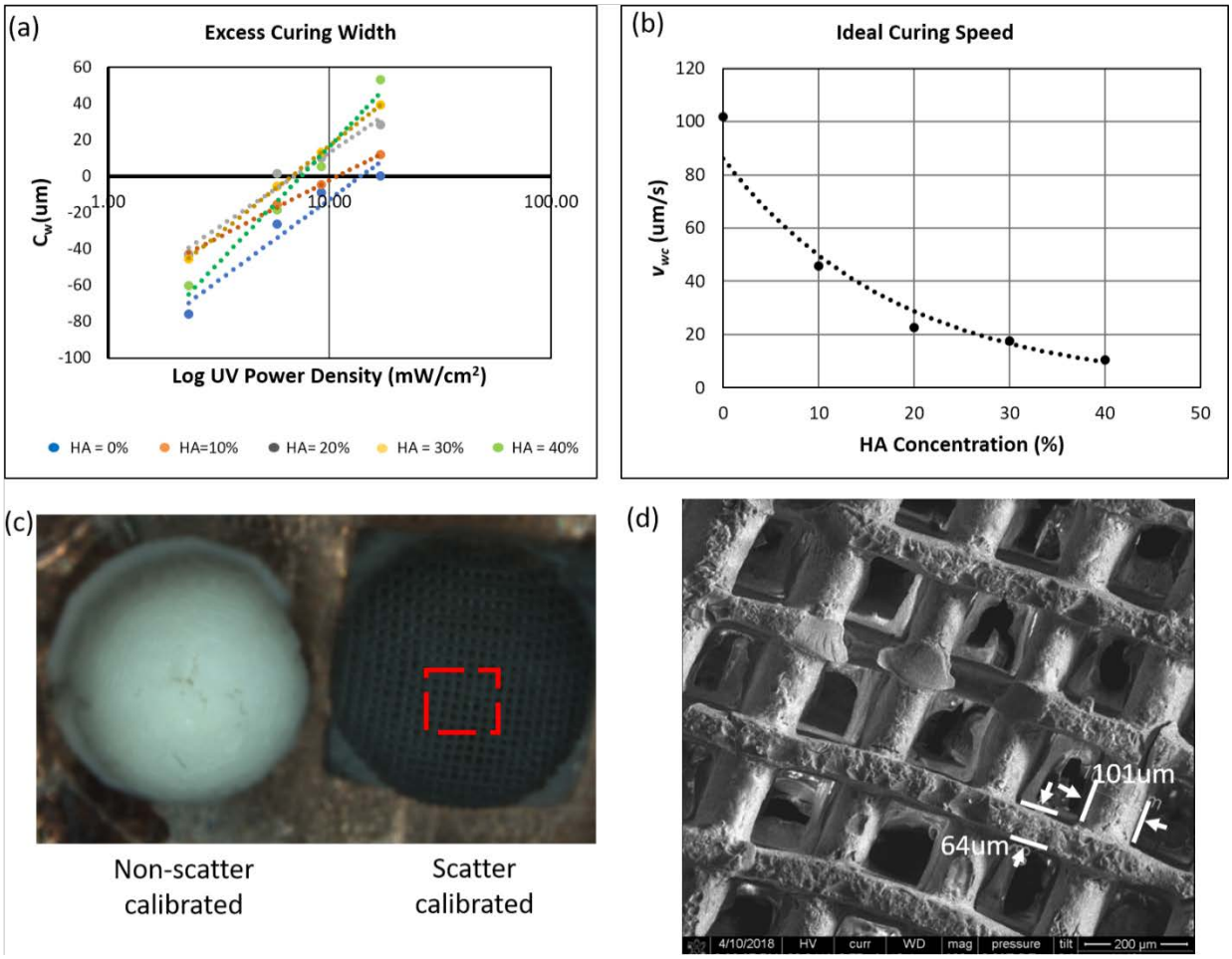

Figure 6: (a) Excess Curing Width (C_w) curves for all tested inks. (b) Critical ideal speed curing curve (c) 3D printed Luneburg lenses printed via microCLIP (20% HA) printed at high intensity high speed and at ideal curing conditions. (d) SEM micrograph of ideal cured Luneburg lens.

Table: Lateral and ideal curing conditions for all tested inks. B_w represents lateral broadening coefficient; P_{wc} represents Power density at onset of broadening; v_{wc} represents the ideal curing speed for dimensional accuracy in terms of axial and lateral dimensions; and Ewc represents ideal curing dosage.

HA Concentration (%)	B_w (um)	P_{wc} (mW/cm^2)	v_{wc} (um/s)	$E_{wc} = P_{wc} * v_{wc}$ (mJ/cm^2)
0	38.7	17.1	101.7	0.84
10	27.2	10.8	45.7	1.19
20	35.7	6.9	22.7	1.53
30	42.3	6.7	17.6	1.91
40	55.6	7.4	10.5	3.52

Discussion

CLIP process is the 3rd generation of stereolithography. microCLIP, in contrast to the scanning and projection stereolithography, integrates oxygen diffusion in the light path to continuously fabricate parts. The photopolymerization is dependent on energy input into the system. If axial curing is the most important criteria for users, there are many UV exposure parameters (UV power and stage speed) that can be employed to attain a desired curing depth (Figure 1). If only axial curing depth is considered, the user has large flexibility in fabrication conditions. It is important to note feature lateral resolution for high resolution applications. The oxygen diffusion in the CLIP process is governed primarily by the photon-flux (UV power density, P_D) through the oxygen permeable membrane, rather than just by total energy dosage ($P_D * t_{exp}$).[2, 11] While axial curing depth is important, lateral calibration for microCLIP for high resolution applications is important. If resin bath and build platform positions are held constant and UV exposure conditions are varied between prints, the lateral print dimensions will also be varied. This is brought about by image blurring along the projected edges, where edge pixels gradually decrease power density depending on oxygen dead zone thickness. This effect can be overcome by offsetting the resin bath and build platform from its initial focus position by the oxygen dead zone thickness.

With the introduction of ceramics into a polymer, lateral dimensional accuracy is of concern immediately. Ceramic-induced light scattering was shown to affect dimensional curing accuracy of the photopolymer ink. With increasing [HA], the lateral broadening coefficient (B_w) increased and axial critical curing energy dosage increased. This is consistent with other works that have utilized stereolithography for ceramic fabrication.[3, 10] Stereolithography users, when utilizing ceramics slurries, must characterize lateral curing and curing depth with respect to energy to determine dimensional accuracy. The user can then utilize the energy dosage at onset of broadening (E_{WC}) to perform the polymerization and remain dimensionally accurate.[3] The introduction of the oxygen dead zone lateral effect causes a “negative” lateral broadening within the excess lateral curing graphs (Figure 6a) which counteracts the scattering brought on from the ceramics. Balancing the two effects yields the ideal curing conditions UV power density and stage speed (P_{wc} , v_{wc}, and E_{wc} respectively) for axial and lateral curing for microCLIP.

An unfortunate downside of the specific dimensionally accurate parameters is this negates fabrication flexibility. Fabrication flexibility is sometimes desired. Typically, higher resolution features are easier to fabricate at lower UV intensities and stage speeds, as the features are subjected to tensile and shear forces and only partial crosslink during printing process. If the ideal curing conditions are relatively high for the desired ink, high resolution features (sub 100um) could be difficult to fabricate. With the characterization methods noted herein, one could modify the projected bitmaps adding/subtracting pixels to offset shrinkage or broadening brought about through the oxygen dead zone and ceramic effects.

Conclusions

microCLIP was used to 3D print parts with varying amounts of ceramic content. Axial Ideal Curing Speed for the tested inks with 20% HA and below resembled a linear increasing relationship with increasing UV power. This indicated that a single UV energy dosage could be used to approximate the dimensionally accurate condition. For inks containing [HA] greater than 20%, the speed working curves resembled a logarithmic relationship in relation to UV power. Lateral curing for all tested inks appeared to have competing effects: oxygen deadzone thickness related defocus and ceramic-induced scattering. From pixel-wise numerical simulation the oxygen-induced defocus could be represented as edge pixels being grayscale or essentially black pixels. In calibration with respect to lateral curing, the excess curing width graph for microCLIP showed that the (-) Y axis represented defocus-dominated feature shrinkage from the oxygen deadzone and the (+) Y axis represented scattering-dominated feature broadening. Critical ideal curing conditions (dimensionally accurate for both axial and lateral curing) could then be obtained from placing the UV power value into the speed working curves, which resulted in a complete exposure condition. Utilizing the ideal curing conditions allowed for high resolution design-intended fabrication.

References

[1]. Guo N and Leu MC, *Additive manufacturing: technology, applications and research needs.* Frontiers of Mechanical Engineering, 2013. **8**(3): p. 215-243.

[2]. Lian Q, Yang F, Xin H, and Li D, *Oxygen-controlled bottom-up mask-projection stereolithography for ceramic 3D printing.* Ceramics International, 2017. **43**(17): p. 14956-14961.

[3]. Halloran JW, *Ceramic stereolithography: additive manufacturing for ceramics by photopolymerization.* Annual Review of Materials Research, 2016. **46**: p. 19-40.

[4]. Cox SC, Thornby JA, Gibbons GJ, Williams MA, and Mallick KK, *3D printing of porous hydroxyapatite scaffolds intended for use in bone tissue engineering applications.* Materials Science and Engineering: C, 2015. **47**: p. 237-247.

[5]. Chen Z, Song X, Lei L, Chen X, Fei C, Chiu CT, Qian X, Ma T, Yang Y, and Shung K, *3D printing of piezoelectric element for energy focusing and ultrasonic sensing.* Nano Energy, 2016. **27**: p. 78-86.

[6]. Jakus AE, Rutz AL, Jordan SW, Kannan A, Mitchell SM, Yun C, Koube KD, Yoo SC, Whiteley HE, and Richter C-P, *Hyperelastic "bone": A highly versatile, growth factor–free, osteoregenerative, scalable, and surgically friendly biomaterial.* Science Translational Medicine, 2016. **8**(358): p. 358ra127-358ra127.

[7]. Bose S, Vahabzadeh S, and Bandyopadhyay A, *Bone tissue engineering using 3D printing.* Materials today, 2013. **16**(12): p. 496-504.

[8]. Trombetta R, Inzana JA, Schwarz EM, Kates SL, and Awad HA, *3D printing of calcium phosphate ceramics for bone tissue engineering and drug delivery.* Annals of biomedical engineering, 2017. **45**(1): p. 23-44.
[9]. Faes M, Valkenaers H, Vogeler F, Vleugels J, and Ferraris E, *Extrusion-based 3D printing of ceramic components.* Procedia CIRP, 2015. **28**: p. 76-81.
[10]. Gentry SP and Halloran JW, *Depth and width of cured lines in photopolymerizable ceramic suspensions.* Journal of the European Ceramic Society, 2013. **33**(10): p. 1981-1988.
[11]. Tumbleston JR, Shirvanyants D, Ermoshkin N, Janusziewicz R, Johnson AR, Kelly D, Chen K, Pinschmidt R, Rolland JP, and Ermoshkin A, *Continuous liquid interface production of 3D objects.* Science, 2015. **347**(6228): p. 1349-1352.
[12]. Van Lith R, Baker E, Ware H, Yang J, Farsheed AC, Sun C, and Ameer G, *3D-Printing Strong High-Resolution Antioxidant Bioresorbable Vascular Stents.* Advanced Materials Technologies, 2016. **1**(9).
[13]. Ware HOT, Farsheed AC, Akar B, Duan C, Chen X, Ameer G, and Sun C, *High-speed on-demand 3D printed bioresorbable vascular scaffolds.* Materials Today Chemistry, 2018. **7**: p. 25-34.
[14]. Bártolo PJ, *Stereolithography: materials, processes and applications*. 2011: Springer Science & Business Media.